METRICA
METRology Institutional CAtalog

ISTITUTO NAZIONALE DI RICERCA METROLOGICA
Repository Istituzionale

Optimizing subtraction-based approaches in time-domain diffuse optics by a time-window analysis

Original
Optimizing subtraction-based approaches in time-domain diffuse optics by a time-window analysis / Di Sieno, L., Pini, E., Martelli, F., Dalla Mora, A.. - In: BIOMEDICAL OPTICS EXPRESS. - ISSN 2156-7085. - 17:11(2026). [10.1364/boe.612321]

Availability:
This version is available at: 11696/90419 since: 2026-10-13T07:51:18Z

Publisher:
Optica Publishing Group

Published
DOI:10.1364/boe.612321

Terms of use:

This article is made available under terms and conditions as specified in the corresponding bibliographic description in the repository

Publisher copyright
Optica Publishing Group (gold)
© XXXX [year] Optica Publishing Group. Users may use, reuse, and build upon the article, or use the article for text or data mining, so long as such uses are for non-commercial purposes and appropriate attribution is maintained. All other rights are reserved.

(Article begins on next page)

03 November 2026

Research Article | Vol. 17, No. 11 / 1 Nov 2026 / Biomedical Optics Express 5557
Biomedical Optics EXPRESS

Optimizing subtraction-based approaches in time-domain diffuse optics by a time-window analysis

LAURA DI SIENO,[1] ERNESTO PINI,[2,3] FABRIZIO MARTELLI,[4] AND ALBERTO DALLA MORA[1,*]

[1]Dipartimento di Fisica, Politecnico di Milano, piazza Leonardo da Vinci 32, 20133 Milano, Italy
[2]Istituto Nazionale di Ricerca Metrologica, strada delle Cacce 91, 10135 Torino, Italy
[3]Laboratorio Europeo di Spettroscopia Non-lineare, via Nello Carrara 1, 50019 Sesto Fiorentino, Italy
[4]Dipartimento di Fisica e Astronomia, Università degli Studi di Firenze, via G. Sansone 1, 50019 Sesto Fiorentino, Italy
[*]alberto.dallamora@polimi.it

Abstract: Diffuse optics measurements performed in the time domain provide the highest information level, but are plagued by a low spatial resolution and significant sensitivity to superficial regions (e.g., extracerebral changes). Here we compare the two main analysis methods (namely, statistical moments and time-windowing of the photon time-of-flight distribution) with the recently introduced dual-slope method. Both in-silico and phantom studies are performed. Our results show that time-windowing, although not previously applied in this context, maximizes the advantages of a dual-slope approach while also maximizing the depth selectivity. Furthermore, for time-windowing, a triple-slope approach is proposed, demonstrating superior rejection of superficial changes.

© 2026 Optica Publishing Group under the terms of the Optica Open Access Publishing Agreement

1. Introduction

Diffuse optical measurements in turbid media are based on the use of near-infrared light to noninvasively assess the absorption (μ_a) and reduced scattering (μ_s') coefficients and their spatial and temporal changes [1]. A plethora of applications benefit from this technique, spanning neurology (e.g., functional brain monitoring) and oncology (e.g., breast cancer), as well as diverse non-biomedical domains [2]. Measurements have been traditionally performed in continuous-wave, frequency-domain, and time-domain modalities, each offering a different trade-off between complexity and performance [1]. Time-domain diffuse optics, in particular, is widely acknowledged as the modality providing the richest information content, despite its greater hardware complexity [3]. However, over the last decade, substantial technological progress has enabled the development of compact, cost-effective, and reliable instruments, thereby broadening their accessibility and translational potential [3–5].

In time-domain diffuse optics a narrow laser pulse is injected into the medium and the re-emitted light is collected by a single-photon detector using the time-correlated single-photon counting technique [6], thus building up a histogram of the distribution of photon times-of-flight (DTOF). The key advantages over other domains are: *i*) the intrinsic independent retrieval of μ_a and μ_s'; *ii*) the photon arrival time encodes penetration depth [3]. These capabilities are particularly relevant for neuroscience, where distinguishing cerebral from extracerebral signals is a critical challenge, and for oncology, where characterizing deep perturbations is of major interest. Indeed, superficial sensitivity can spoil the information coming from deep tissues.

Time-domain diffuse optics measurements are typically performed with a source-detector distance of about 2-3 cm, which limits the spatial resolution of the investigation as the probed region into the medium has the so-called "banana" shape, where the two ends of the banana

#612321 https://doi.org/10.1364/BOE.612321
Journal © 2026 Received 22 Jul 2026; revised 17 Sep 2026; accepted 22 Sep 2026; published 7 Oct 2026

Biomedical Optics EXPRESS

are anchored at the source and detector positions on the surface of the medium, while the rest of the banana extends below the sample surface. Although small or even null source-detector distances can enhance the confinement of the probed volume in the medium [7] by changing the sensitivity shape from banana-like to drop-like, the technical complexity of such measurements (e.g., requiring a fast transition from the OFF to the ON state of the detector) has hindered their widespread use. In the last decade, the so-called single-slope (SS) approach based on spatial subtraction between two slightly displaced collection points (e.g., 5 mm) has been proposed [8]. In this way, a new observable is created, with reduced sensitivity to unknown multiplicative factors such as coupling and source power, as well as to contributions that are similarly sensed by both source–detector pairs. Indeed, when two closely spaced collection points are combined by subtraction, the resulting sensitivity map becomes, conceptually, the difference between the two individual sensitivity maps. As a consequence, a SS acquisition tends to exhibit a low or even null sensitivity to regions of the tissue that are sampled in a similar way by both channels, whereas the sensitivity is enhanced in regions where one of the two source–detector pairs is comparatively more sensitive than the other.

Operating in the time domain, in 2016 Milej et al. [8] introduced this concept by demonstrating that the SS approach enables retrieval of the optical properties of the bottom layer of a bilayer sample with an error of about 10%. However, phantom validation revealed greater uncertainty than the traditional approach due to higher noise induced by subtraction. In the same year, Milej et al. demonstrated that the SS method improves penetration, accuracy and depth selectivity within layered turbid media when short source-detector distances are used [9] and also reported the first *in-vivo* validation. However, both phantom and *in-vivo* experiments confirmed a larger variability of the results with a SS approach.

In 2019, a double subtraction method was proposed (i.e., the so-called dual-slope -DS- approach) in both time-domain (with data analysis limited to the use of statistical moments) [10] and frequency-domain [11] modalities to preserve the improved depth selectivity of the SS approach, while mitigating the increased variability caused by subtraction. In DS, two closely displaced collection fibres are placed in the centre of a probe, between two source fibres positioned symmetrically on either side, so that the same near and far source–detector separations are realized in a mirror configuration. Hence, two SS observables are computed, and the final DS observable is obtained by averaging the two SS ones. The combination of two mirrored SS sensitivity maps can suppress residual asymmetries due to channel-dependent coupling, while retaining reduced sensitivity to superficial/common-mode contributions. These studies reported a more confined sensitivity shape in the medium, leading to enhanced depth selectivity and lateral resolution compared with classical single-distance approach. In 2021, the DS approach was validated also in the continuous-wave regime, demonstrating calibration-free retrieval of optical properties [12,13]. Initial *in-vivo* frequency-domain studies by Blaney et al. suggested that the DS approach attenuates superficial (i.e., extracerebral) signal contamination [14,15]. These encouraging results were followed by other *in-vivo* investigations [16–18]. Beyond improved depth discrimination, the DS method can also reduce the effects of motion artifacts, as well as the imperfect tissue-optode contact. Consistent results were obtained also in the time-domain in 2023 by Fazliazar et al., who observed a residual superficial sensitivity and an increased noise contribution with subtraction-based methods [19]. Collectively, these results emphasize the growing relevance of slope-based strategies as promising techniques towards more robust and clinically viable diffuse optical measurements, adhering to the broader effort of the scientific community to improve non-invasive tissue diagnostics.

It is worth noting that all the time-domain studies here reviewed employed statistical moments analysis of DTOFs (namely, attenuation, average time and variance, see Ref. [20]), whereas time-window (TW) analysis (i.e., integrating the DTOF within selected temporal gates to analyse only photons arriving in a given early, middle or late time range, see Ref. [21]), though not yet

Biomedical Optics EXPRESS

applied to subtraction-based measurements, is recognized for offering higher contrast and superior depth selectivity, at the expense of a stronger dependence on the instrument response function shape and its possible temporal drifts [21]. A rigorous comparison between these analysis strategies is therefore not only technically relevant but also crucial for guiding the design and validation of next-generation time-domain diffuse optics instruments, and translation to clinical practice. The aim of this work is to compare the two analysis methods within a DS configuration and identify the most suitable approach for optimizing the benefits of subtraction-based strategies while minimizing the impact of noise. We employ Monte Carlo simulations to mimic a localized perturbation at various positions within the probed medium. Complementary phantom tests with a totally absorbing perturbation are conducted to provide experimental validation. By addressing this gap through quantitative performance metrics established in the field of diffuse optics [22], the present study seeks to inform not only specialists in the field but also the broader biomedical and clinical communities, interested in advancing portable, non-invasive, and accurate optical technologies for tissue monitoring and diagnostics.

2. Materials and methods

2.1. Monte Carlo simulations

Monte Carlo (MC) simulations were performed with the GPU implementation of Monte Carlo eXtreme (MCX) [23] on a workstation equipped with an NVIDIA Quadro RTX 6000 graphics card (24 GB VRAM), in order to match the conditions of the phantom experiments (see Section 2.2). The computational domain reproduces the black polyvinyl chloride (PVC) tank in which the experimental phantom measurements are performed (see Fig. 1(a); $W \times H \times D = 120 \times 170 \times 65\ mm^3$). It is discretized on a Cartesian grid with 0.5-mm voxels. This voxel size was selected as a compromise between geometric fidelity of the ~5 mm inclusion and computational burden. Additional tests with finer voxelization produced no appreciable differences in the resulting contrast maps, while increasing the runtime. Two pencil-beam sources (S1 and S2) are placed at $x = \pm 27.5$ mm ($y = 0$, $z = 0$) and launched along the $+z$ direction, while two circular detection (D1 and D2) areas (radius 0.5 mm) are defined at $x = -2.5$ mm (D1) and $x = +2.5$ mm (D2). Time-resolved DTOFs are generated over a 12.5-ns window using 2048 time bins ($\Delta t \approx 6.1$ ps).

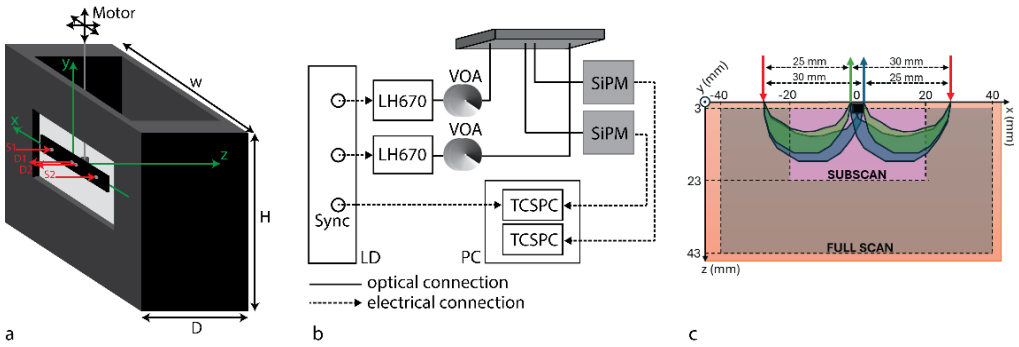


Fig. 1. Scheme of the phantom tank (a), experimental setup (b), and scheme of the different scans (c, subscan -pink area- and full scan -brown area-).

To enable the extensive scan grids required in this work, simulations are implemented using a photon-replay strategy. A single "seed" simulation with 10^{12} photons is first run in the homogeneous medium, and the random seeds together with the detected-photon packets are stored separately for each source (S1, S2) and detector (D1, D2). For each perturbation position, Monte Carlo eXtreme replay mode is then used by re-injecting the stored seeds and detected-photon

Biomedical Optics EXPRESS

packets while updating only the voxelized volume of the perturbation. The perturbation is modelled as a black PVC cylinder (~100 mm^3; height and diameter ~5 mm) positioned at the same x, y and z coordinates as in the experimental scans; the voxel inclusion is defined by a voxel-center criterion. To compensate for voxelization artifacts, the cylinder radius is calibrated so that the resulting discretized volume remains consistent with the target nominal volume. The initial homogeneous seed run required approximately 90 h. Thereafter, each replay-based simulation for a fixed-y plane, with the perturbation scanned over the corresponding xz grid, required about 10 h.

The effect of the black perturbation in the Monte Carlo simulations is implemented using a photon-removal strategy, discarding detected photons whose path intersects the defect volume. This choice provides a practical and stable way to emulate a highly absorbing inclusion within the photon-replay framework and yields an upper-bound perturbation effect compared with a finite $\Delta\mu_a$ perturbation. While simplified, this strategy was adopted consistently across all simulated conditions and was primarily intended to enable a controlled comparison among the different data-reduction pipelines. Although the nominal geometry, volume, and scan coordinates of the experimental inclusion were reproduced, the photon-removal model assumes an ideal, perfectly absorbing object. Therefore, possible residual discrepancies between simulations and measurements may also arise from deviations of the actual inclusion geometry and positioning from the idealized model, in addition to instrumental noise and phantom drifts. Background absorption is included in the simulations ($\mu_a = 0.05\ cm^{-1}$), and the resulting DTOFs were convolved with the measured instrument response function to replicate the experimental timing response. The optical properties and the measured instrument response function used in the simulations matched the 670 nm phantom experiment. Finally, to reproduce realistic counting statistics, simulated DTOFs are scaled so that the homogeneous condition matches the measured count rates (i.e., about 600 kcps and 2 Mcps -megacounts per seconds- for the two separations as detailed in Sect. 2.2), and Poisson noise is applied. For each case, ten statistically independent simulations are run using the same procedure as in the phantom experiments.

2.2. Phantom experiments

In the experimental setup (Fig. 1(b)), two high-power diode lasers (LDH-P-C-670M laser heads -LH-, driven by PDL 828 Sepia II, Picoquant GmbH, Germany -LD-) provide 670 nm pulses at a 40 MHz repetition rate, which are directly coupled to step-index optical fibres with a 600 μm core diameter and a numerical aperture of 0.22. The laser driver is set to deliver a pulse from the second laser head at about 12.5 ns delay from the pulse emitted by the first laser head. Each fibre is pigtailed to a different U-bracket, in which the optical beam propagates in free space. A variable optical attenuator (VOA, round continuously-variable neutral density filter by Thorlabs Inc., USA) is inserted in this section of each U-bracket to adjust the injected power level not to significantly exceed limitations of single-photon statistics in time-correlated single-photon counting. The output of each U-bracket is pigtailed to another optical fibre with identical characteristics of the input one. The output fibre of each U-bracket is then connected to a step index optical fibre with a 1 mm core and a numerical aperture of 0.39, which is inserted into a custom probe and serves as the injection fibre for the diffusive medium. The distance between the two injection fibres in the probe is 55 mm. Two identical 1 mm core and 0.39 numerical aperture optical fibres are connected to the same probe to serve as collection fibres. These fibres are positioned at 25 and 30 mm from the injection points (see Fig. 1(c)). As a result, the injection-collection geometry follows that proposed in both Refs. [10,19] (i.e., to the best of our knowledge, the only time-domain dual slope studies performed so far, both based on moment analysis), since the purpose of this work was not to optimize the probe layout but to compare DTOF observables under a previously validated and optimized dual-slope configuration. The probe is constructed from black PVC and covered, on the phantom side, with a thin adhesive

Biomedical Optics EXPRESS

black velvet tape to suppress direct light propagation between injection and detection points. The velvet layer is removed beneath the fibres tips to ensure optimal optical coupling with the sample. On the other side, the two collection fibres are connected to two custom large-area single-photon detectors (upgraded from [24], now based on a S13362-1350DG silicon photomultiplier -SiPM-, Hamamatsu Photonics K.K., Japan), which generate electrical pulses upon photon detection. These pulses were sent to the stop input of two time-correlated single-photon counting (TCSPC) boards (SPC130, Becker & Hickl GmbH, Germany) installed in a personal computer. The start signal for both boards is provided by the laser synchronism output. It is worth noting that, because of the 12.5 ns delay between the two laser heads, on a time-scale of 25 ns each histogram shows 2 DTOFs. In this way, it is possible to distinguish between photons injected in x = -27.5 mm and those injected in x = + 27.5 mm (see Fig. 1(c)).

The diffusive medium consists of a liquid phantom prepared by mixing calibrated quantities of water, India ink, and Intralipid, to achieve optical properties of $\mu_a = 0.05\,\mathrm{cm}^{-1}$ and $\mu_s' = 10\,\mathrm{cm}^{-1}$ [25]. An absorbing inclusion is moved within the phantom using a computer-controlled motorized stage (see Fig. 1(a)). The inclusion is a black 100 mm^3 volume PVC cylinder with height and diameter of about 5 mm. Its effect has been demonstrated to be equivalent to $\Delta\mu_a = 0.17\,\mathrm{cm}^{-1}$ over a volume of 1 cm^3 [26]. The liquid phantom is contained inside a black PVC tank with a lateral Mylar window for optical access, on which the probe is placed.

Two measurements are performed. A first measurement (subscan) is done to simultaneously evaluate contrast and its coefficient of variation (CV). This requires the acquisition of multiple DTOFs for each perturbation position, resulting in a relatively long acquisition time. Preliminary tests (data not shown) indicated that the phantom's optical properties varied by about 1% over 1 hour most likely due to particle deposition. Therefore, this first measurement is restricted to a small scanning area (i.e., "subscan" in Fig. 1(c)) to perform a complete scan in about 1 hour. In this case, the perturbation y position was fixed at $y = 0$ mm (i.e., where the centre of the perturbation moves along an ideal line connecting together all the centres of the optical fibres, see Fig. 1(a)), while along the x axis (i.e., lateral scan) it was scanned from -20 to 20 mm, in 2 mm steps ($x = 0$ mm corresponding to the midpoint between the two collection fibres). Along the z axis (i.e., depth scan), it is moved from 3 mm (i.e., the top of the perturbation is located just 0.5 mm below the probe) to 23 mm, also in 2 mm increments. For each step, ten histograms composed by two different DTOFs at 12.5 ns relative delay are recorded with 2 s acquisition time each. As shown in Fig. 1, each detector collects light from 2 injection fibers, one placed at 25 mm and another one at 30 mm of source-detector separation. The variable optical attenuators are set to obtain a photon counting rate of about 1 Mcps in each histogram referred to the 25 mm distance and of about 300 kcps in each histogram at 30 mm distance (i.e., overall about 1.3 Mcps per timing board, corresponding to 3.25% of the laser repetition rate). In terms of signal-to-noise ratio, a 2 s acquisition time measurement at 1 Mcps (300 kcps) can be considered equivalent to a 1 s acquisition time one performed with a photon counting rate of 2 Mcps (600 kcps), that is the simulated scenario.

The second measurement (full scan) aims to visualize the sensitivity profile with a larger field of view by also changing the y position of the perturbation, without evaluating the CV. This procedure involves acquiring 2D images in the x-z plane at different y positions. To minimize optical properties drifts, each acquisition is limited to a single x-z plane, after which the phantom is stirred and re-measured at a new y position. Because only one histogram composed by two different DTOFs is collected per position instead of ten, the scanned area is expanded while keeping the overall measurement time for one x-z plane in the order of 1 hour. In this case the perturbation is moved along the y axis from 0 to 14 mm in 2 mm steps, along the x axis from −40 to 40 mm in 2 mm steps, and along the z axis from 3 to 43 mm in 2 mm steps. As for the subscan case, the acquisition time is set to 2 s and the variable optical attenuators are set to obtain a photon counting rate of about 1.3 Mcps per timing board.

Biomedical Optics EXPRESS

2.3. Data analysis

To allow a fair comparison between measurements and simulations, the same MATLAB-based code (whose main steps are described in the following) is applied to each DTOF (starting point reported as "Raw DTOF Data" in Fig. 2).

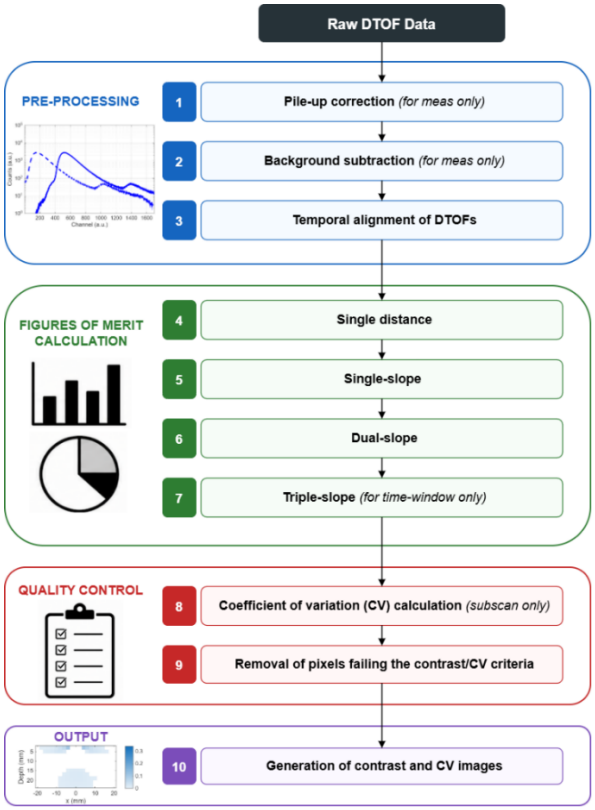


Fig. 2. Workflow of the data analysis used to generate the contrast and, for the subscan, also CV images.

It is well known and widely discussed in the literature that time-correlated single-photon counting measurements enable reliable optical pulse reconstructions provided that the photon counting rate is kept much lower (~1%, see Ref. [3]) than the laser pulse rate. Beyond that, suitable correction methods must be implemented to avoid detrimental effects from the so- called pile-up distortion. Since our photon counting rate of about 1.3 Mcps per timing board is >3% of the laser rate, we apply the pile-up correction through the Coates algorithm (step 1 in Fig. 2), which has been demonstrated to be effective for diffuse optics measurements [27]. After pile-up correction, the constant background due to detector noise was subtracted from each DTOF (step 2 in Fig. 2). Its value was computed as the mean level of the noise before each DTOF peak. However, only 85% of the background is subtracted to ensure avoiding over-subtractions which may distort the DTOF shapes. Both pile-up correction and background subtraction are avoided for Monte Carlo simulations, being pile-up and background free.

For both measurements and simulations we apply a shift to the instrument response function so as to have its peak in the first time bin of the DTOF histogram by subtracting its peak position delay to shift the entire histogram. The same shift is also applied to all the DTOFs to keep relative temporal distance between the instrument response function and the DTOFs unchanged

Biomedical Optics EXPRESS

(step 3 in Fig. 2). In this way statistical moment and time-windowing analysis can be applied avoiding effects from mismatch in the electrical cables or optical fibres length.

After the pre-processing steps, for both measurements and simulations, different figures of merit (FOMs) are computed to compare the depth sensitivity achieved using TW-based analysis and with moment-based approach (step 4 in Fig. 2). For the TW analysis, for each source-detector distance and for each point of the scan (pixel), we compute the contrast in different TWs positions (defined with respect to the instrument response function peak). The TWs are 1000 ps width, starting about 180 ps after the instrument response function peak and with no overlap between them. The contrast (C) for each n-th TW (TW_n) is computed for each point of the scan in the following way:

$$C(TW_n) = \log_{10}\left(\frac{N_0(TW_n)}{N(TW_n)}\right) \tag{1}$$

where $N_0(TW_n)$ and $N(TW_n)$ are the number of counts in the homogeneous (i.e., the perturbation is moved apart on the opposite side with respect to the injection fibre considered) and in the heterogeneous (i.e., the perturbation is inside the field of view of the scan depicted in Fig. 1) case in the n-th TW, respectively. We adopt base-10 logarithms to express TW contrasts in decadic attenuation (optical-density-like) units. Since these observables are used only as experimental contrast metrics computed from measured and simulated DTOFs, and not to retrieve absolute optical properties through an analytical diffusion model, changing to natural logarithms would only rescale them by the constant factor $\log_e(10)$.

We then compute the difference between the long source-detector distance and the short one (i.e., we calculate the so-called SS, which corresponds to step 5 in Fig. 2) and the dual slope contrast (step 6 in Fig. 2) by averaging the SS results (as reported in Ref. [19]):

$$\Delta C_{SS,S1} = C_{S1-D2} - C_{S1-D1} \tag{2}$$

$$\Delta C_{SS,S2} = C_{S2-D1} - C_{S2-D2} \tag{3}$$

$$\Delta C_{DS} = \frac{1}{2}(\Delta C_{SS,S1} + \Delta C_{SS,S2}) \tag{4}$$

where $\Delta C_{SS,j}$ are the SS contrasts computed for j-th source, C_{j-k} are the contrast computed for the single source (j)-detector (k) distance and ΔC_{DS} is the dual slope contrast.

Wabnitz et al. [21], for classical single-distance measurements (i.e., not spatial subtraction based), demonstrated clear advantages in computing the differential contrast between different TWs. To the best of our knowledge, this method has never been explored for dual-slope acquisitions. Specifically, we compute the difference between the DS contrasts obtained in two adjacent time windows (ΔTW), TW_{n+1} and TW_n, where n denotes the earlier one. As a best compromise between depth penetration and CV, we use $n = 2$, corresponding to $TW_3 - TW_2$. Indeed, $n = 1$ would lead to a reduced penetration because of the use of early-arriving photons, while $n = 3$ would lead to CV > 1 for most of the points of the scans because of the low photon rate within such late gates. This additional level of subtraction is hereinafter referred to as triple slope (TS, step 7 in Fig. 2).

To cope with the larger contrast contribution of the superficial layer as compared to deeper regions, only a portion α of TW_n is subtracted, with α computed for each case to cancel out the superficial contrast in the central pixel, thus potentially maximizing the depth selectivity. The α factor is independently computed for simulations and measurements in the subscan case and applied to both subscan and full scan, since the subscan features a better signal-to-noise ratio due to the tenfold acquisition time per pixel. The α factor is therefore a predetermined local condition, neither the deep signal nor the entire map is optimized, computed by looking for the best possible rejection of the superficial contrast contributions. In fact, the TS contrast is defined as $\Delta C_{TS} = \Delta C_{DS}(TW_{n+1}) - \alpha\, \Delta C_{DS}(TW_n)$. In the present proof-of-principle study,

Biomedical Optics EXPRESS

α is determined by imposing zero TS contrast at the predefined superficial reference position $x = 0$ mm, $z = 3$ mm. Therefore, α is determined as $\alpha = \Delta C_{DS}(TW_{n+1}) \,/\, \Delta C_{DS}(TW_n)$ evaluated at $x = 0$ mm, $z = 3$ mm. Thus, α is not obtained by optimizing the entire contrast map or maximizing the recovered deep signal. For a future *in-vivo* implementation, α should be determined independently of the physiological response under investigation, for example through a prior superficial calibration made on phantom or a model-based estimate and subsequently kept fixed during the measurement. The use of representative/average parameter values determined experimentally is common in biomedical optics. For example, the differential path length factor is commonly used in continuous-wave measurements to estimate changes in tissue absorption, and heuristic expressions for calculating its values as a function of wavelength and age in humans can be found in the literature. Following a similar approach, it would be reasonable to construct a table of values for α covering a range of wavelengths and optical properties representative of the intended application values. Developing and validating such a calibration procedure is beyond the scope of the present study and represents an important direction for future work.

In the statistical moments analysis, each DTOF is reduced to three observables (step 4 in Fig. 2): attenuation (A), mean time of flight (*TMean*), and variance (*Var*). These quantities are computed over the same temporal range used for the TW analysis (all time bins outside the region covered by TWs are set to zero). Importantly, these observables do not have the same physical dimension: similarly to contrast (C), A is dimensionless by construction, whereas *TMean* and *Var* have units of time and time squared, respectively. Therefore, before applying subtractions, *TMean* and *Var* have to be converted into relative changes with respect to the corresponding unperturbed values, so as to obtain dimensionless contrast-like quantities directly comparable with attenuation and contrast.

For A, we apply the definition (see, for example, Ref. [19]):

$$A = \log_{10}\left(\frac{N_0}{N}\right) \tag{5}$$

and we also compute the SS (i.e., the difference for each source between the long and the short source-detector distance, step 5 in Fig. 2) and the DS (step 6 in Fig. 2) [19]:

$$\Delta M_{i,SS,S1} = \Delta M_{i,S1-D2} - \Delta M_{i,S1-D1} \tag{6}$$

$$\Delta M_{i,SS,S2} = \Delta M_{i,S2-D1} - \Delta M_{i,S2-D2} \tag{7}$$

$$\Delta M_{i,DS} = \frac{1}{2}(\Delta M_{i,SS,S1} + \Delta M_{i,SS,S2}) \tag{8}$$

where i is the order of the statistical moment (i.e., $i = 0$ for attenuation), $\Delta M_{i,SS,j}$ is the SS of the i-th moment computed for j-th source, $\Delta M_{i,j-k}$ are the i-th moment differences between the homogeneous and perturbed cases for the single source (j)-detector (k) distance and $\Delta M_{i,DS}$ is the DS of the i-th moment.

For *TMean* and *Var*, we start from the definition for the single distance case (SD) [19]:

$$\Delta M_{i,SD} = M_{i,SD,HOMO} - M_{i,SD,PERT} \tag{9}$$

where $i = 1$ for *TMean* and $i = 2$ for *Var*, and subscripts HOMO and PERT respectively refer to the homogeneous (i.e., no perturbation in the field of view) and perturbed cases.

As previously mentioned, perturbation-induced changes in *TMean* and *Var* have to be expressed as fractional variations with respect to the unperturbed values. For both *TMean* and *Var*, after computing their SS values using Eq. (6),(7) we normalize them by the mean value over the 10 repetitions and two source-detector distances of the *TMean* and *Var* computed in the homogeneous

Biomedical Optics EXPRESS

case for each source (i.e., $TMean_{SS_j,0}$ and $Var_{SS_j,0}$), as follows:

$$FOM(TMean_{SS_j}) = \frac{TMean_{SS_j}}{TMean_{SS_j,0}} \tag{10}$$

$$FOM(Var_{SS_j}) = \frac{Var_{SS_j}}{Var_{SS_j,0}} \tag{11}$$

After normalization, the DS figures of merit are computed as [19]:

$$FOM(TMean_{DS}) = \frac{\left(\frac{TMean_{SS_1}}{TMean_{SS_1,0}} + \frac{TMean_{SS_2}}{TMean_{SS_2,0}}\right)}{2} \tag{12}$$

$$FOM(Var_{DS}) = \frac{\left(\frac{Var_{SS_1}}{Var_{SS_1,0}} + \frac{Var_{SS_2}}{Var_{SS_2,0}}\right)}{2} \tag{13}$$

For the subscan, where the 10 repetitions of the same measurements are available, the average value and standard deviation for each FOM (TW contrast and its difference -ΔTW-, A, $TMean$ and Var) are computed. This allows us to calculate the CV to determine the statistical robustness of the FOM (step 8 in Fig. 2). Pixels where CV is higher than 1, being statistically non-significant, are removed from the maps reporting results. In the same way, for both full scan and subscan, all pixels where the absolute value of the FOM is lower than 1% (i.e., usually considered the minimum significant contrast for *in-vivo* measurements as compared to biological fluctuations) are removed (step 9 in Fig. 2).

3. Results and discussion

3.1. Subscan

Figure 3 shows the outcome of Monte Carlo simulations for the subscan. Each subplot pertains to the contrast/CV produced by a localized perturbation as a function of the depth (z) and lateral (x) position, at fixed y = 0 mm. Each row of plots focuses on a different figure of merit, in particular, rows 1 to 4 show the contrast computed in different consecutive TWs, row 5 shows the contrast of ΔTW, while the last 3 rows show, in order, the three moments A, $TMean$, and Var. Since subtraction-based techniques typically generate both regions of positive (i.e., where an increase of absorption due to the perturbation produces an increase in contrast) and negative (i.e., where an increase of absorption produces a decrease in contrast) sensitivity, the two polarities are separately plotted in the two columns, thus allowing us to use the same colour scale for comparison purposes. As expected, by considering TWs moving from early (TW1) to late (TW4) times it is possible to probe deeper regions of the sample, also reducing the superficial contrast (the maximum value goes from 66.7% in TW1 to 22.0% in TW4). The negative contrast region represents an undesired behaviour in subtraction-based techniques and it is often not clearly studied (e.g., in [19] colour scales are saturated in the negative sensitivity region to focus only on the positive one). In this case, for TWs, it presents lower contrasts, especially on the surface of the sample, thus implying a greater contribution from positive contrast, as expected.

Remarkably, the addition of a third level of subtraction (ΔTW in Fig. 3) generates a positive sensitivity that is almost completely independent of superficial changes, with maximum sensitivity at a depth of 7 mm (3.8%) and with almost completely absent negative sensitivity. This could lead, for instance, to *in-vivo* measurements of brain imaging with superior rejection of superficial (systemic extracerebral) changes or to improved independence of skin tone for oximetry. Unfortunately, as it is already known for the first and second ones [8,9,19], also the third level of subtraction produces an increase in the noise level (and therefore an increase in the CV).

Biomedical Optics EXPRESS

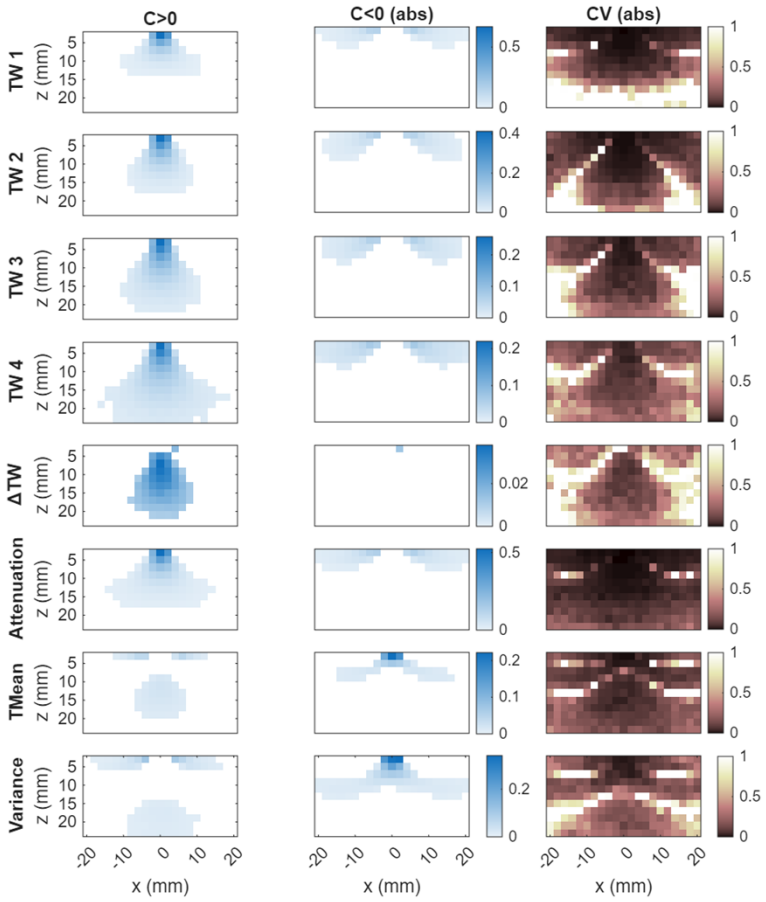


Fig. 3. Simulation: contrast and CV produced by localized perturbation as a function of the depth (z) and lateral (x) position with DS technique considering different TWs and ΔTW (5 top rows of plots) and moment analysis (3 bottom rows of plots). Left and central columns of plots respectively report only regions of positive contrast and the absolute value of negative contrast. The right column reports the CV.

The weighting factor α compensates for the different superficial responses measured in adjacent time windows. As described in Section 2.3, its value is fixed by imposing zero TS contrast at the predefined superficial reference position and is therefore not obtained by optimizing either the deep signal or the overall contrast map. An intuitive reason why this subtraction works pretty well in rejecting surface contributions can be understood by noting that, for a very thin surface layer, the path travelled in that layer by detected photons is approximately twice the layer thickness and almost independent of the arrival time at the detector site. Thus, a variation in the optical properties inside a voxel belonging to this layer will produce an attenuation variation independent of the arrival time at the detector site.

Concerning moment analysis, in line with theory, A shows a behaviour close to TW analysis (maximum contrast of 52.4% at $z = 0$ mm) since it is equivalent to it if considering a single large time window including the whole DTOF (i.e., equivalent to continuous wave measurements).

It is well known (see for instance Ref. [21]) that, to reach deep tissue structures, *TMean* and *Var* are the most meaningful moments. Indeed, although they exhibit lower contrast values (e.g., 2.2% at $z = 13$ mm and 1.7% at $z = 21$ mm, respectively), both moments show a localized

Biomedical Optics EXPRESS

deep sensitivity spot, at depths increasing with the moment order. However, an undesired residual superficial sensitivity is always present in the positive contrast case (maximum values are about 4.5% and 11%, respectively), as also clearly described in the literature (see e.g., [17]). Furthermore, by looking at the negative polarity of contrasts, it is possible to notice an undesired strong superficial sensitivity (maximum values of 22.2% and 34.1%, respectively), which is substantially larger than the average deep sensitivity, thus reducing the penetration. This would imply both the presence of confounding effects during brain imaging measurements (e.g., a decrease in the blood content in the scalp could give a large contribution in the same direction of a deep brain activation) and high sensitivity to skin tone in oximetry measurements.

Figure 4 shows the results of the experimental campaign with the same plot structure of Fig. 3. Generally speaking, all the considerations already drawn for simulations are here confirmed. Some sensitivity shapes are not perfectly balanced creating asymmetrical sensitivity in some plots. Deep localized sensitivity spots are smaller than in simulations for the TS approach, as well as for *TMean* and *Var*. While asymmetries may arise from imperfectly balanced detector count rates, the reason for the reduction of the spot size is straightforward since real measurements are not only affected by Poisson noise as considered in simulations, but also by other noise sources like laser power fluctuations or drifts. Hence, in real cases the CV is generally higher than in simulations, thus reducing the number of significant points in the plots. Despite these differences, the advantages of TW analysis are clearly confirmed by measurements, and in particular for the case of TS technique, where the point of maximum sensitivity is at a depth of 11-13 mm (2%), with no significant surface contribution in either the positive or negative sensitivity maps.

TMean and *Var* exhibit a deep sensitivity of 1.6% at 13 mm and 1.5% at 19 mm depth respectively, but the superficial contrast again largely overcomes these numbers both in the positive (2.7% and 4.2%, respectively) and in the negative (10.3% and 12.7%, respectively) sensitivity cases.

Overall, results coherently indicate that TW analysis can enhance the depth selectivity of the DS approach, motivating the introduction of a TS extension to further suppress superficial contributions.

3.2. Full scan

Considering the clear advantage of the triple slope approach with TW analysis, we now focus the results presentation and discussion on this approach for the full scan case, in comparison with moment analysis. This full-scan acquisition allows us to identify possible undesired surface-localized sensitivity spots close to the injection fibres, i.e., a region that was excluded from the subscan investigation, in order to keep the total measurement time below 1 hour.

Figure 5 reports, in columns from left to right, the simulated positive polarity of contrasts for ΔTW, A, *TMean,* and *Var*. The corresponding negative polarity ones are reported in Fig. 6. For both figures, each plot shows the effect of a localized perturbation as a function of the depth (z) and lateral (x) position. Different y positions are reported in different rows of plots.

In agreement with the subscan case, at $y = 0$ mm, the maximum sensitivity of ΔTW is not superficial, but at a depth of 7 mm (~4%). It is worth noting that in this case the drop-like contrast shape is slightly more irregular. This is expected since, despite being performed at the same count rate as the subscan, for the full scan just 1 measurement of 2 s per point is taken, while in the subscan case, to enable the use of the CV to validate the statistical significance of each pixel in the map, 10 repetitions of 2 s are taken, resulting in 10 times more photons at all arrival times. In the negative sensitivity plot for the $y = 0$ mm case, generally speaking, there is a single point of sensitivity (<1.1%, hence slightly above the 1.0% threshold on contrast, at $z = 5$ mm), most probably due to the high noise of the full-scan and the absence of a data validation threshold on the CV.

Biomedical Optics EXPRESS

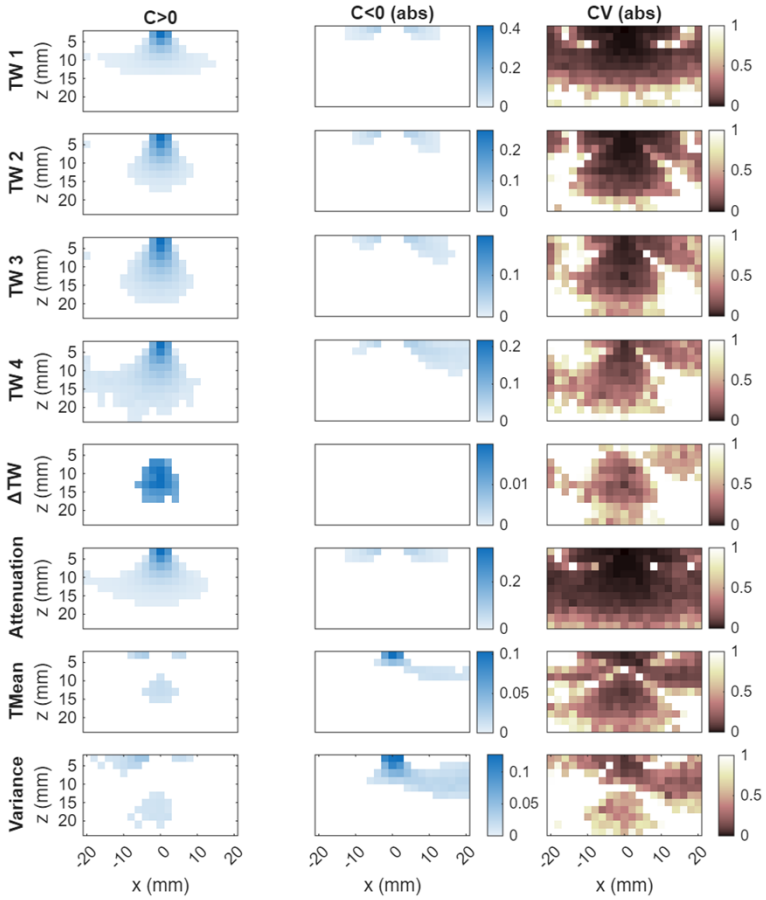


Fig. 4. Measurement: contrast and CV produced by localized perturbation as a function of the depth (z) and lateral (x) position with DS technique considering different TWs and ΔTW (5 top rows of plots) and moment analysis (3 bottom rows of plots). Left and central columns of plots respectively report only regions of positive contrast and the absolute value of negative contrast. The right column reports the CV.

By moving the perturbation to higher y values, as expected, the sensitivity spots are progressively smaller and the perturbation is no longer detectable beyond $y = 12$ mm for the positive sensitivity case. Therefore, we can estimate that the spatial resolution (full-width at half maximum) along the y direction is about 12 mm for the TS approach.

For A moment analysis, the spatial resolution is almost identical along the y direction, but both sensitivity polarities are clearly peaked at $z = 0$ mm (52.2% and 13.1%, respectively), generating sensitivity to extracerebral changes or to skin tone in case of *in-vivo* measurements.

As concerns *TMean*, the spatial resolution along the y direction is slightly better than for the TS case, as the perturbation is lost after $y = 10$ mm, while for *Var* it is slightly worse than the TS case because the perturbation is barely detectable also at $y = 14$ mm, although the statistical significance of these points is unclear because CV information is not available. However, for both *TMean* and *Var*, the maximum contrast (for $y = 0$ mm) is at $z = 0$ mm for both positive (4.7% and 10.9%, respectively) and negative (22.1% and 33.0%, respectively) cases, while the sensitivity in the deep spot of the positive sensitivity is considerably lower (2.2% at $z = 11$ mm and about 2.4% at $z = 17$ mm, respectively). Hence, the maximum negative sensitivity is about 5 and 3 times

Biomedical Optics EXPRESS

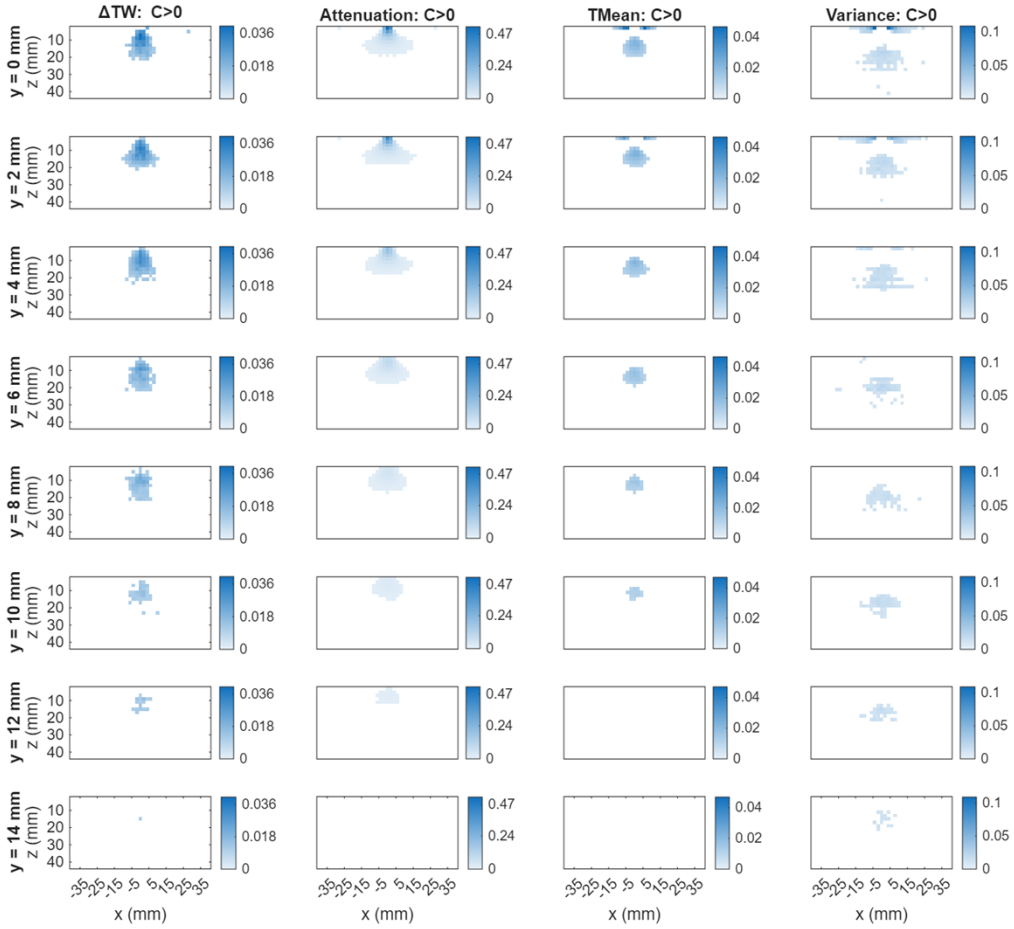


Fig. 5. Simulation: contrast (only positive polarity) produced by localized perturbation as a function of the depth (z) and lateral (x) position with TS technique by ΔTW analysis and DS with moment analysis measurables (columns) at different y planes (rows).

larger than the maximum positive sensitivity for *TMean* and *Var*, respectively, introducing strong influence of superficial tissues in case of *in-vivo* measurements.

The corresponding full scan experimental results are reported in Fig. 7 and Fig. 8, respectively showing the positive and negative polarities of the same measurables displayed in Fig. 5 and Fig. 6, following the same data structure.

For ΔTW, the maximum contrast at $y = 0$ is superficial (4.6% at $z = 0$ mm, under one of the source fibres), while the sensitivity in the deep spot of the positive sensitivity is about 3% around $z = 11$ mm. In the negative sensitivity case the maximum value of contrast is 5.9% at $z = 0$ mm. Concerning the y resolution, the perturbation is still barely visible at $y = 10$ mm, while the contrast points at $y = 12$ mm are probably not significant.

In the A moment analysis, results appear less affected by noise, as expected because of the use of the whole photon distribution for its calculation and the perturbation is clearly lost after $y = 10$ mm. At $y = 0$ mm, the maximum positive contrast is 40.7% and the negative one is 19.4%, both at $z = 0$ mm.

Biomedical Optics EXPRESS

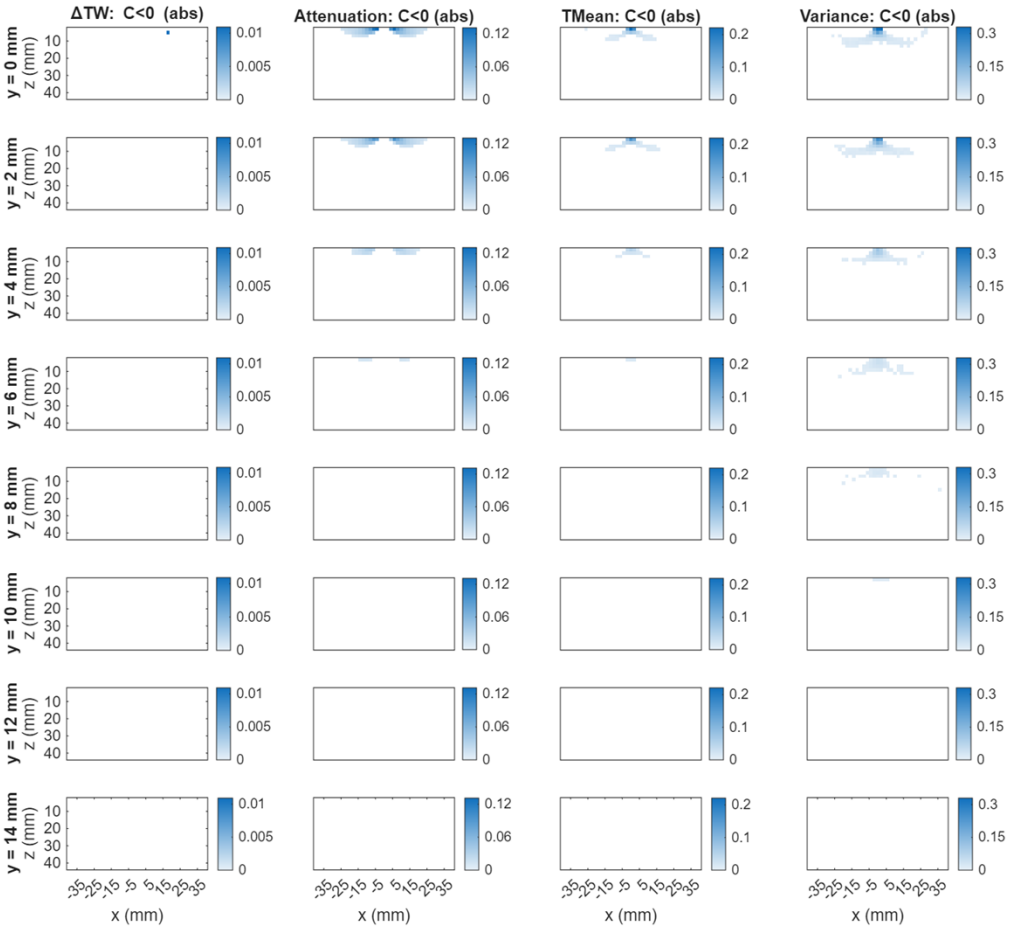


Fig. 6. Simulation: contrast (only negative polarity) produced by localized perturbation as a function of the depth (z) and lateral (x) position with TS technique by ΔTW analysis and DS with moment analysis measurables (columns) at different y planes (rows).

For *TMean*, experiments suggest a spatial resolution along the y direction of about 8 mm, while *Var* is slightly worse because the perturbation seems to be barely detectable up to about y = 12 mm, however the actual detectability remains unclear because of the lack of the CV information. While simulations reported ratios between the maximum negative sensitivity and the maximum positive sensitivity at the surface of about 5 and 3 for *TMean* and *Var*, respectively, experimental results are slightly better since these ratios are respectively reduced to about 3 (positive: 5.3%, negative: 16.8%) and 1 (positive: 26.0%, negative: 30%). The maximum deep positive sensitivity for *TMean* is 2% at z = 13 mm, while for *Var* is about 3.1% at z = 19 mm. Hence, in both cases it is confirmed that the maximum sensitivity is superficial.

In order to quantitatively compare statistical moment and TW analysis methods, from results reported in Fig. 3–8, we compute the contrast-weighted mean depths ($\langle z_{CW} \rangle$) by averaging the depth coordinate using the local contrast as weighting factor over the contrast map. This is done for both area scan types and considering two different cases: *i*) only positive contrast maps and *ii*) both signs of contrast (absolute values). Results are reported in Table 1. For the simulated subscan case and considering both contrast polarities, it is possible to appreciate that penetration slightly increases, as expected, with the order of the statistical moment from 6.6 mm for *A* to

Biomedical Optics EXPRESS

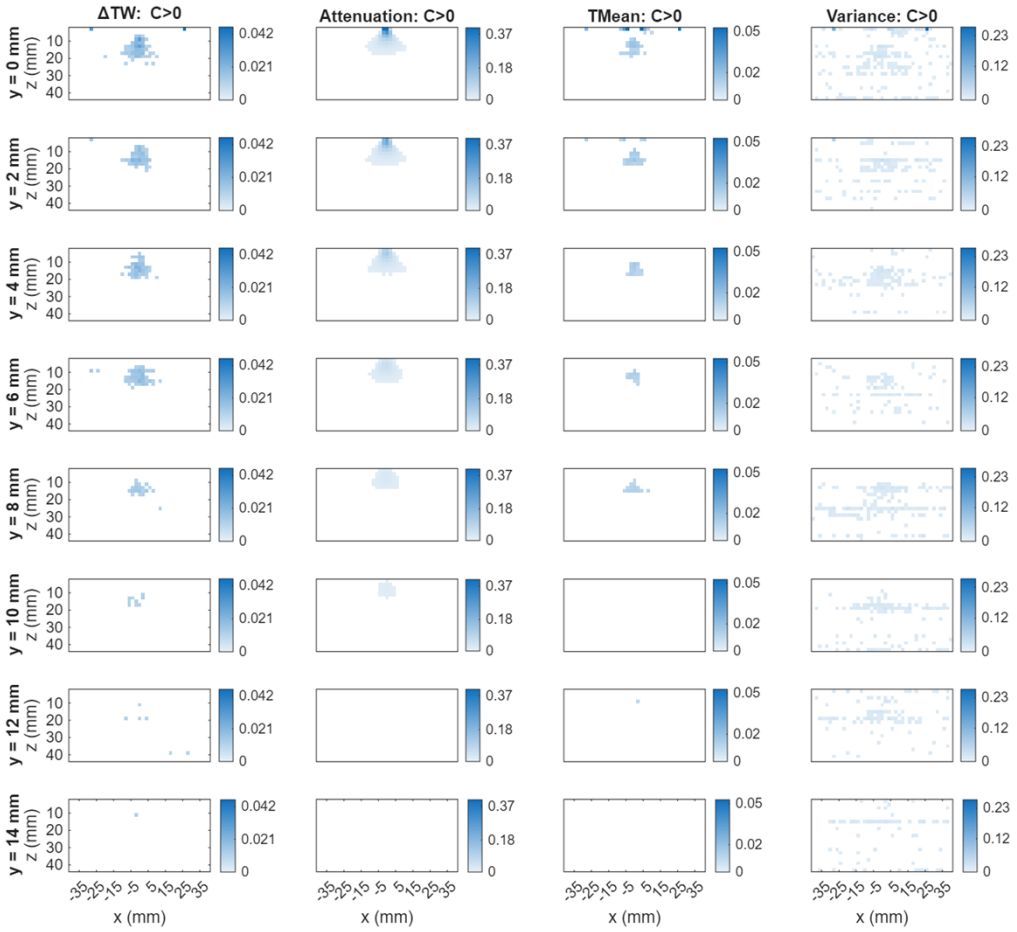


Fig. 7. Measurement: contrast (only positive polarity) produced by localized perturbation as a function of the depth (z) and lateral (x) position with TS technique by ΔTW analysis and DS with moment analysis measurables (columns) at different y planes (rows).

7.6 mm for *Var*. If considering only the positive contrast regions, $\langle z_{CW} \rangle$ is 0.9–3.3 mm larger. However, during an *in-vivo* application of brain imaging, when extracerebral confounding effects may materialize by both increasing or decreasing absorption, the superficial sensitivity (which typically presents a negative sign) can hinder the detection of deep changes. Therefore, excluding negative sensitivity regions to compute $\langle z_{CW} \rangle$ may be inappropriate. Instead, ΔTW analysis allows us to reach a $\langle z_{CW} \rangle$ that is at least 4.8 mm larger than any other statistical moment and almost independent of the considered contrast polarity. Measured values of $\langle z_{CW} \rangle$ are not far from simulated ones, with a maximum difference of just 1.2 mm when considering both polarities. As concerns the full scan, statistical moments are in good agreement with the subscan, with a maximum difference of 0.7 mm if excluding *Var* and considering both polarities. Indeed, the measured $\langle z_{CW} \rangle$ of 14.1 mm for *Var* should not be considered a significant number since, as it is clear from Figs. 8, there are many contrast points up to the maximum depth that are just due to the larger noise as compared to the subscan. Conversely, this issue is largely reduced, but not completely absent, in simulations, and the average penetration of the full scan is 1.1 mm larger than the subscan if considering both polarities, which is probably minimally overestimated. The

Biomedical Optics EXPRESS

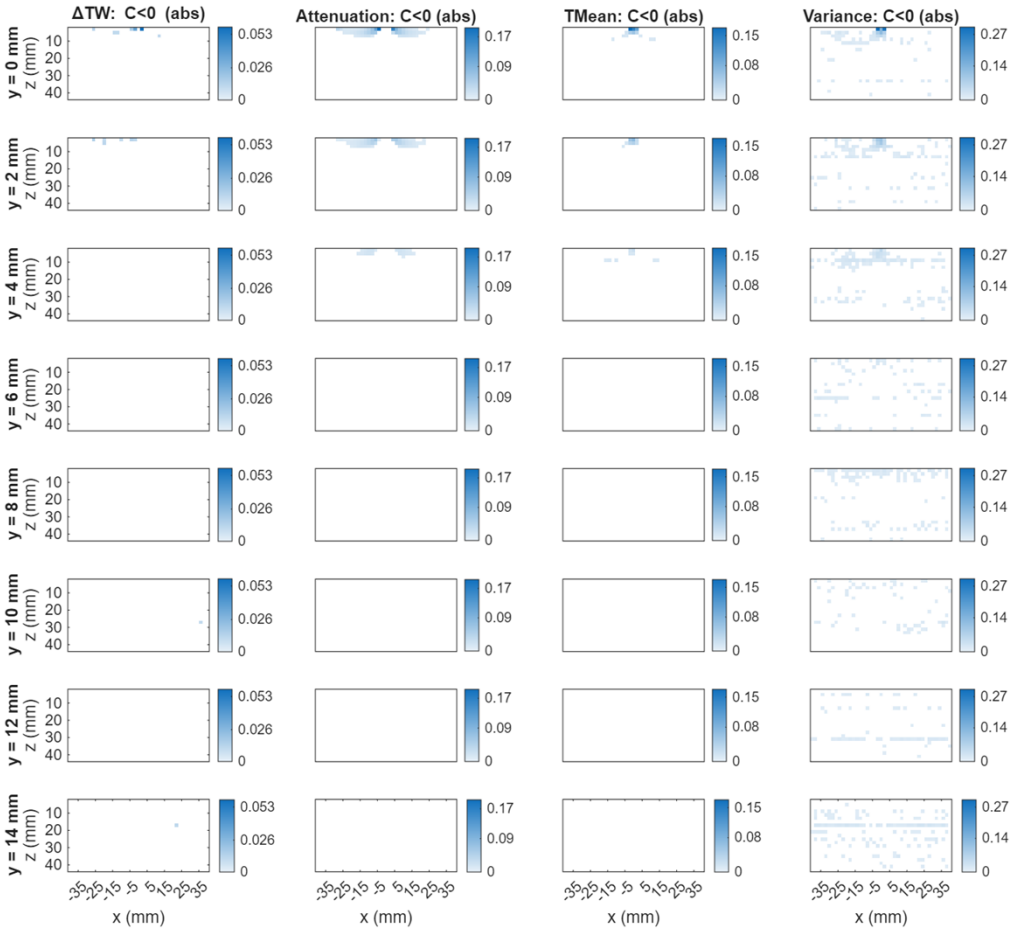


Fig. 8. Measurement: contrast (only negative polarity) produced by localized perturbation as a function of the depth (z) and lateral (x) position with TS technique by ΔTW analysis and DS with moment analysis measurables (columns) at different y planes (rows).

ΔTW analysis of the full scan exhibits a deeper penetration if compared with A and $TMean$, with a maximum discrepancy of 1.3 mm if compared with the subscan case.

For a quantitative evaluation of the depth selectivity (s_z) and its dependence on the four different observables (O), namely, ΔTW, A, $TMean$, and Var, we compute the ratio:

$$s_z = \frac{\sum_{x=min}^{max} \sum_{z=3}^{43} |O(x,z)| \; - \; \sum_{x=min}^{max} \sum_{z=3}^{7} |O(x,z)|}{\sum_{x=min}^{max} \sum_{z=3}^{43} |O(x,z)|} \times 100 \tag{14}$$

for both area scan types. In this way, s_z can range from 0% (in the extreme case of null sensitivity beyond a depth of 7 mm) to 100% (in case of null superficial sensitivity). For the purpose of this metric, the region $z \leq 7$mm was defined as superficial, as it can represent a reasonable scalp-dominated depth range in a functional brain measurements scenario. Results are reported in Table 2. For both subscan and full scan it is evident that statistical moments exhibit a depth selectivity much lower than ΔTW, with good agreement between simulations and measurements. Generally speaking, the full scan exhibits a reduced selectivity if compared with the subscan case,

Biomedical Optics EXPRESS

Table 1. Values of contrast-weighted mean depths (z_{CW}) expressed in mm obtained with TW (only ΔTW is reported) and statistical moment (attenuation, average time and variance) analysis for both simulations (Sims) and measurements (Meas) and both scanning geometries (subscan and full scan). Within brackets are reported values obtained considering only the positive contrast.

		ΔTW	A	TMean	Var
Subscan	Sims	12.4	6.6	7.1	7.6
		(12.5)	(7.5)	(10.4)	(10.2)
	Meas	12.1	7	6.3	7.5
		(12.1)	(7.7)	(9.1)	(9.3)
Full Scan	Sims	12.2	6.6	7.1	8.7
		(12.3)	(7.6)	(10.3)	(12.7)
	Meas	11.9	6.3	6.2	14.1
		(13.4)	(7.4)	(8.6)	(18.0)

but this is expected because of the higher noise and the extension of the scan to the superficial region under the injection fibres.

Table 2. Depth selectivity values obtained with TW (only ΔTW is reported) and statistical moment (attenuation, average time and variance) analysis for both simulations (Sims) and measurements (Meas) and both scanning geometries (subscan and full scan).

		ΔTW	A	TMean	Var
Subscan	Sims	81%	29%	34%	35%
	Meas	89%	36%	30%	37%
Full Scan	Sims	79%	29%	34%	38%
	Meas	72%	25%	27%	52%

Overall, the triple slope approach demonstrates clear advantages in terms of average penetration depth and superficial information rejection. It is worth noting that this method requires no modification of the acquisition hardware and introduces negligible computational overhead, just requiring a subtraction between two numbers already computed in the classical TW analysis. However, because of the subtraction between Poisson-dominated measurables, the noise contribution increases, as is already known to happen in the single- and dual-slope computations [8,9,19]. A further point to consider is that, in the field of time-domain diffuse optics, the feasibility of adopting photon count rates approaching the laser repetition one has been demonstrated, avoiding pile-up distortion by applying the Coates' data correction algorithm [27], thus boosting the signal-to-noise ratio. Hence, we speculate that the increased noise of subtraction-based techniques can be compensated in the future by adopting a high-throughput system.

Since this study presents the first comparison between statistical moment and time-window analysis with subtraction based techniques applied between adjacent injection and collection positions, it is worth pointing out its main limitations. First, it only considers a single geometry with 25 and 30 mm inter-fiber distances, while future studies should address other arrangements to expand our conclusions. Second, the CV is not studied for full scan measurements since this would have increased the drift of phantom optical properties well beyond 1%. Solid phantoms could have represented a valid alternative, however currently available phantoms are only suitable for 2D scans [28]. Third, the α factor is here determined through a predefined local cancellation condition. Further investigations are required to establish a calibration or model-based procedure

Biomedical Optics EXPRESS

for determining α in a real world application, independently of the physiological response under investigation.

4. Conclusions

This paper reports an investigation on the effect of different distribution of photon times-of-flight data reduction techniques on depth sensitivity and selectivity in dual-slope measurements of time-domain diffuse optics. Both Monte-Carlo simulations and phantom experiments demonstrate that a differential time-window analysis (i.e., the proposed triple slope approach) consistently provides a substantially larger contrast-weighted penetration depth and depth selectivity than the statistical-moment observables.

Overall, extending the dual-slope acquisition to a triple-slope strategy by combining information coming from two delayed time windows can provide near-complete superficial rejection without sacrificing deep-target visibility. Therefore, it represents a practical solution toward robust suppression of extracerebral contributions in brain monitoring and of skin-related confounding factors in muscle oximetry.

Funding. European Union (D2B8D520).

Disclosures. The authors declare no conflicts of interest.

Data availability. Data underlying the results presented in this paper are available at Ref. [29].

References

1. T. Durduran, R. Choe, W. B. Baker, *et al.*, "Diffuse optics for tissue monitoring and tomography," Rep. Prog. Phys. **73**(7), 076701 (2010).
2. T. D. O'Sullivan, H. Dehghani, and R. Re, "Diffuse Optical Spectroscopy: Technology and Applications: Introduction to the Feature Issue," Biomed. Opt. Express **15**(11), 6516–6520 (2024).
3. A. Pifferi, D. Contini, A. Dalla Mora, *et al.*, "New frontiers in time-domain diffuse optics, a review," J. Biomed. Opt. **21**(9), 091310 (2016).
4. L. Di Sieno, G. Maffeis, A. Dalla Mora, *et al.*, "Smart Optode for 8-Wavelength Time-Gated Diffuse Optics," IEEE J. Sel. Top. Quantum Electron. **30**(1), 1–9 (2024).
5. H. Y. Ban, G. M. Barrett, A. Borisevich, *et al.*, "Kernel Flow: a high channel count scalable time-domain functional near-infrared spectroscopy system," J. Biomed. Opt. **27**(07), 074710 (2022).
6. R. H. Hadfield, "Single-photon detectors for optical quantum information applications," Nat. Photonics **3**(12), 696–705 (2009).
7. A. Pifferi, A. Torricelli, L. Spinelli, *et al.*, "Time-Resolved Diffuse Reflectance Using Small Source-Detector Separation and Fast Single-Photon Gating," Phys. Rev. Lett. **100**(13), 138101 (2008).
8. D. Milej, A. Abdalmalak, D. Janusek, *et al.*, "Time-resolved subtraction method for measuring optical properties of turbid media," Appl. Opt. **55**(7), 1507–1513 (2016).
9. D. Milej, A. Abdalmalak, P. McLachlan, *et al.*, "Subtraction-based approach for enhancing the depth sensitivity of time-resolved NIRS," Biomed. Opt. Express **7**(11), 4514–4526 (2016).
10. P. Sawosz and A. Liebert, "Method to improve the depth sensitivity of diffuse reflectance measurements to absorption changes in optically turbid medium," Biomed. Opt. Express **10**(10), 5031–5041 (2019).
11. A. Sassaroli, G. Blaney, and S. Fantini, "Dual-slope method for enhanced depth sensitivity in diffuse optical spectroscopy," J. Opt. Soc. Am. A **36**(10), 1743–1761 (2019).
12. G. Blaney, P. Curtsmith, A. Sassaroli, *et al.*, "Broadband absorption spectroscopy of heterogeneous biological tissue," Appl. Opt. **60**(25), 7552–7562 (2021).
13. G. Blaney, R. Donaldson, S. Mushtak, *et al.*, "Dual-Slope Diffuse Reflectance Instrument for Calibration-Free Broadband Spectroscopy," Appl. Sci. **11**(4), 1757 (2021).
14. G. Blaney, C. Fernandez, A. Sassaroli, *et al.*, "Dual-slope imaging of cerebral hemodynamics with frequency-domain near-infrared spectroscopy," Neurophotonics **10**(01), 1–22 (2023).
15. G. Blaney, C. Fernandez, A. Sassaroli, *et al.*, "Dual-slope diffuse optical imaging with a modular source-detector array," Neural Imaging and Sensing 2023, Proc. SPIE **12365**, 1 (2023).
16. A. Kılıç, G. Blaney, F. Tavakoli, *et al.*, "Frequency-domain instrument with custom ASIC for dual-slope near-infrared spectroscopy," Rev. Sci. Instrum. **95**(11), 114706 (2024).
17. G. Blaney, J. Frias, F. Tavakoli, *et al.*, "Dual-ratio approach to pulse oximetry and the effect of skin tone," J. Biomed. Opt. **29**(S3), 1–25 (2024).
18. C. Fernandez, G. Blaney, J. Frias, *et al.*, "Single-distance and dual-slope frequency-domain near-infrared spectroscopy to assess skeletal muscle hemodynamics," J. Biomed. Opt. **28**(12), 1–19 (2023).
19. E. Fazliazar, A. Sudakou, P. Sawosz, *et al.*, "Depth-selective method for time-domain diffuse reflectance measurements: validation study of the dual subtraction technique," Biomed. Opt. Express **14**(12), 6233–6249 (2023).

Biomedical Optics EXPRESS

20. H. Wabnitz, A. Jelzow, M. Mazurenka, *et al.*, "Performance assessment of time-domain optical brain imagers, part 2: nEUROPt protocol," J. Biomed. Opt. **19**(8), 086012 (2014).
21. H. Wabnitz, D. Contini, L. Spinelli, *et al.*, "Depth-selective data analysis for time-domain fNIRS: moments vs. time windows," Biomed. Opt. Express **11**(8), 4224–4243 (2020).
22. L. Hacker, H. Wabnitz, A. Pifferi, *et al.*, "Criteria for the design of tissue-mimicking phantoms for the standardization of biophotonic instrumentation," Nat. Biomed. Eng. **6**(5), 541–558 (2022).
23. Q. Fang and S. Yan, "MCX Cloud—a modern, scalable, high-performance and in-browser Monte Carlo simulation platform with cloud computing," J. Biomed. Opt. **27**(08), 083008 (2022).
24. E. Martinenghi, L. Di Sieno, D. Contini, *et al.*, "Time-resolved single-photon detection module based on silicon photomultiplier: A novel building block for time-correlated measurement systems," Rev. Sci. Instrum. **87**(7), 073101 (2016).
25. L. Spinelli, M. Botwicz, N. Żołek, *et al.*, "Determination of reference values for optical properties of liquid phantoms based on Intralipid and India ink," Biomed. Opt. Express **5**(7), 2037–2053 (2014).
26. F. Martelli, P. D. Ninni, G. Zaccanti, *et al.*, "Phantoms for diffuse optical imaging based on totally absorbing objects, part 2: experimental implementation," J. Biomed. Opt. **19**(7), 076011 (2014).
27. E. Avanzi, A. Behera, D. Contini, *et al.*, "Effects and correctability of pile-up distortion using established figures of merit in time-domain diffuse optics at extreme photon rates," Sci. Rep. **12**(1), 5417 (2022).
28. A. Pifferi, A. Torricelli, R. Cubeddu, *et al.*, "Mechanically switchable solid inhomogeneous phantom for performance tests in diffuse imaging and spectroscopy," J. Biomed. Opt. **20**(12), 121304 (2015).
29. L. Di Sieno, E. Pini, F. Martelli, *et al.*, "Optimizing subtraction-based approaches in time-domain diffuse optics by a time-window analysis," Zenodo, 2026, https://doi.org/10.5281/zenodo.19232144